Journal of
Materials Chemistry A

PAPER

View Article Online
View Journal | View Issue

Cite this: J. Mater. Chem. A, 2018, 6, 13075

Received 10th April 2018
Accepted 25th May 2018

DOI: 10.1039/c8ta03270j

rsc.li/materials-a

P3-type $K_{0.32}Fe_{0.35}Mn_{0.65}O_2\cdot 0.39H_2O$: a promising cathode for Na-ion full batteries†

Sai Wang,[a] Yun-hai Zhu,[a] Jun-min Yan *[a] and Xin-bo Zhang [b]

Na-ion batteries (NIBs) are very attractive candidates for large-scale electrical energy storage due to abundant Na resources, while developing air stable, low cost and toxic Co/Ni-free cathodes to achieve high energy/power density and long-life NIBs is very challenging. Herein, as a proof-of-concept experiment, rare P3-type $K_{0.32}Fe_{0.35}Mn_{0.65}O_2\cdot 0.39H_2O$ (KFM) made from environmentally friendly and low cost elements is first proposed and demonstrated to be a novel cathode for NIBs. Unexpectedly, the KFM exhibits outstanding electrochemical performances including high specific capacity (137.5 mA h g^{-1}), rate capability and coulombic efficiency (*ca.* 100%), and long cycle stability (1000 cycles). Furthermore, a highly efficient prototype NIB was first realized using this KFM cathode and a Na_x–Sb_2O_3 anode, which shows high energy density and power density (220.5 W h kg^{-1}; 4340 W kg^{-1}) even with high round-trip energy efficiency (*ca.* 100%) and excellent cycling stability (over 900 cycles).

Introduction

The integration of renewable intermittent energy into the electrical grid calls for low-cost and efficient batteries with superior energy storage ability,[1,2] wherein Na-ion batteries (NIBs) have recently been widely proposed as very promising due to their environmental friendliness and the worldwide distribution of sodium (Na) resources.[3–8] Though NIBs share the same 'rocking chair' working principle as Li-ion batteries (LIBs), it is still a significant challenge to develop cathode materials to accommodate Na ions with a larger radius (1.02 Å), as well as to ensure a long lifespan during the rapid and repeated Na ion insertion/desertion processes.[9–14] Layered sodium transition metal oxides that crystallize in P2 and O3 polymorphs with the general formula Na_xMeO_2 (Me: transition metal) have attracted intensive research interest due to the electrochemical/reversible intercalation of Na.[15,16] Nevertheless, the air instability of almost all the Na_xMeO_2 materials (prone to react with water/carbon dioxide molecules) and necessary incorporation of expensive and toxic Co/Ni into the Me layer to achieve good performance terribly hinder their practical application.[17–21] Therefore, developing low-cost, Co/Ni-free and air-stable cathodes with high capacity and long cycling life is urgently desired but remains a great challenge.

Herein, as a proof-of-concept experiment, we first propose and demonstrate that a novel layered transition-metal oxide, $K_{0.32}Fe_{0.35}Mn_{0.65}O_2\cdot 0.39H_2O$ (KFM, a representative example of the big P3-type K_xMeO_2 family), holds great promise as a low-cost, Co/Ni-free and air-stable cathode for NIBs. Unexpectedly, the KFM with an inter-planar distance over 7 Å shows a surprising Na ion storage ability, including high specific capacity (137.5 mA h g^{-1}), high coulombic efficiency (CE) (*ca.* 100%), and superior cycling stability (1000 cycles). Furthermore, when coupled with an un-optimized Na_x–Sb_2O_3 anode, a prototype NIB exhibits high energy and power densities (220.5 W h kg^{-1}; 4340 W kg^{-1}), a round-trip energy efficiency of *ca.* 100%, and excellent cycling stability (over 900 cycles even at a high energy density of 1000 mA g^{-1}).

Furthermore, the structural changes of KFM during cycling were also investigated by *ex situ* X-ray diffraction. Interestingly, the result indicates that the P3-type structure converts to a P3 substitution (similar to Na_xMeO_2), and the undesirable multiple irreversible phase transitions observed in P2 and O3-type Na_xMeO_2 have not happened. Given the cost-effectiveness, air stability, and big family of Ni/Co-free KFM, the promising results presented here would open new avenues and inspire more research interests on novel P3-type K_xMeO_2 cathodes for next generation NIBs.

Experiments

Materials synthesis and characterization

P3-type $K_{0.32}Fe_{0.35}Mn_{0.65}O_2\cdot 0.39H_2O$ (KFM) was prepared by a handy sol–gel method. 1.021 g CH_3COOK, 1.010 g $Fe(NO_3)_3\cdot 9H_2O$, 1.225 g $Mn(CH_3COO)_2\cdot 4H_2O$ and 8.416 g citric acid were mixed and stirred uniformly in 50 ml deionized water. Then the solution was transferred to a clean glass dish and heated at 90 °C for 12 hours to form a foam gel. The gel was then removed from the dish and heated at 380 °C for 5 hours and further

---

[a] Key Laboratory of Automobile Materials, Ministry of Education, Department of Materials Science and Engineering, Jilin University, Changchun, 130012, P. R. China. E-mail: junminyan@jlu.edu.cn

[b] State Key Laboratory of Rare Earth Resource Utilization, Changchun Institute of Applied Chemistry, Chinese Academy of Sciences, Changchun, 130022, P. R. China

† Electronic supplementary information (ESI) available. See DOI: 10.1039/c8ta03270j

heated at 800 °C for another 5 hours in a muffle furnace without a temperature-fall period. The heating rates were all set to 5 °C min^{-1} for the two temperature-rise periods. After being cooled in air, the as-obtained ash was washed with deionized water and ethyl alcohol several times by centrifugation to remove the soluble by-products. The wet powders were dried at 80 °C overnight in an oven.

Characterization

A Bruker D8 Focus Powder X-ray diffractometer with Cu Kα radiation (40 kV, 40 mA) was employed to perform the X-ray diffraction (XRD) measurements and then the XRD data were refined through the Rietveld method (GSAS program suite). An ESCALAB MK II was utilized to obtain X-ray photoelectron spectroscopy (XPS) data. A Thermo Jarrell Ash (TJA) Atomscan Advantage instrument was utilized to perform inductively coupled plasma-atomic emission spectroscopy (ICP-AES) measurements. Scanning electron microscopy (SEM) images were collected on a field emission Hitachi S-4800 instrument. Elemental mapping and transmission electron microscopy (TEM) were both conducted on a FEI Tecnai G_2 S-Twin instrument. Thermogravimetric analysis (TGA) was performed from 25 to 500 °C at a heating rate of 10 °C min^{-1} under an air atmosphere through a NETZSCH STA 449 F3 Simultaneous TGA-DSC Instrument. The *ex situ* XRD patterns were collected from KFM electrodes of different charge/discharge depths that were pre-sealed in sample holders with Kapton film windows in argon to avoid contact with air.

Electrochemical evaluation

The electrodes were fabricated by spreading the slurries containing 70 wt% of active materials, 20 wt% of acetylene black and 10 wt% of CMC binder on aluminum foil (KFM) or copper foil (Sb_2O_3) by the doctor blade method, and the electrodes were dried at 80 °C for 12 hours. The mass loading of KFM and Sb_2O_3 on the current collector was about 1 and 1.1 mg cm^{-2}, respectively. The electrodes were then cut into 12 mm diameter discs and coin-type (CR2025) cells were assembled with pure sodium foil as the counter electrode and glass fibers as the separator in an argon-filled glovebox. The electrolyte was 1 M $NaPF_6$ in EC/DEC (1 : 1 v/v) with 5% FEC. For assembling Na-ion full batteries, the Sb_2O_3 electrodes were pre-sodiated to 0 V (*vs.* Na^+/Na) to get the matching anodes which contain a Na–Sb alloy and Na_2O. There was not any treatment of the KFM cathodes and the specific capacity was calculated based on the mass of the cathode (cathode-limited type). Galvanostatic charge/discharge tests were carried out on a Land CT2001A battery testing system (Land, China). Cyclic voltammetric measurements were conducted at a scan rate of 0.1 mV s^{-1} using a VMP3 electrochemical workstation (Bio-Logic, France).

Results and discussion

The P3-type KFM was prepared *via* a facile and mild sol–gel method in an air atmosphere, using low cost CH_3COOK, $Fe(NO_3)_3 \cdot 9H_2O$ and $Mn(CH_3COO)_2 \cdot 4H_2O$ as precursors, citric acid as the chelating ligand and deionized water as the solvent. As the adsorbed water and structured water often exist together in the K-containing layered transition metal oxides,[22,23] thermogravimetric analysis (TGA) is employed and the weight loss (water content) around 160 °C is about 6.5% (Fig. 1). The KFM after a similar heating procedure to TGA was also characterized by XRD measurements (500 °C, 10 °C min^{-1} and 10 min holding time). No other phase could be observed and thus it's inferred that only water was removed and no other phase transition happened during the TGA process (Fig. S1†). The atomic ratio of K, Fe and Mn is then determined to be 0.32 : 0.35 : 0.65 using inductively coupled plasma-atomic emission spectroscopy (ICP-AES). According to the above results and the general formula A_xMeO_2 (A represents an alkali metal ion), the chemical formula of the as-synthesized sample is $K_{0.32}Fe_{0.35}Mn_{0.65}O_2 \cdot 0.39H_2O$.

The purity of KFM is then investigated by X-ray diffraction (XRD) and the corresponding Rietveld refinement method as shown in Fig. 2a. It can be seen that all the Bragg diffraction peaks are in excellent agreement with the Rietveld refinement results, indicating the high purity of the KFM sample. The space group is indexed to $R3m$ and the refined lattice parameters of KFM are $a = b = 2.8927$ Å, $c = 21.0291$ Å, $\alpha = \beta = 90°$ and $\gamma = 120°$ ($R_{WP} = 6.73\%$, $R_p = 3.62\%$, and $\chi^2 = 3.629$). The lattice reflections, inter-planar distances, peak intensities and atomic positions obtained through refinement are listed in Tables S1 and S2.† The original model used for Rietveld refinement is $Na_{0.6}CoO_2$ (Inorganic Crystal Structure Database (ICSD) code: 9992). And the constraint in the process of refining this ideal model is that the K atom and the water molecule are restricted to the same position. From the corresponding crystal structure determined from the refinement result (Fig. 2b), it is observed that different from the common P2 and O3 type structures, the KFM crystallizes in a rare P3-type structure with an AABBCC oxygen packing.[24] As all the trigonal prismatic polyhedra in the P3 structure are equivalent and are all built by the same number of atoms,[25] the marked representative trigonal prismatic positions between the transition metal–oxygen sheets in Fig. 2b are all possible intercalated sites for potassium ions.

To determine in which step during the synthesis water was formed, the XRD patterns of the as-obtained ash before the

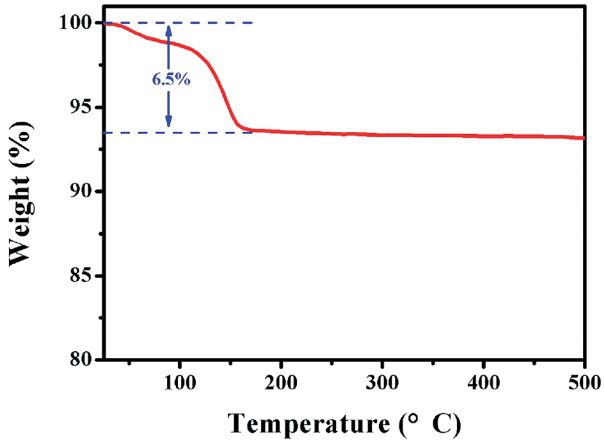

Fig. 1 TGA curve of the KFM sample.

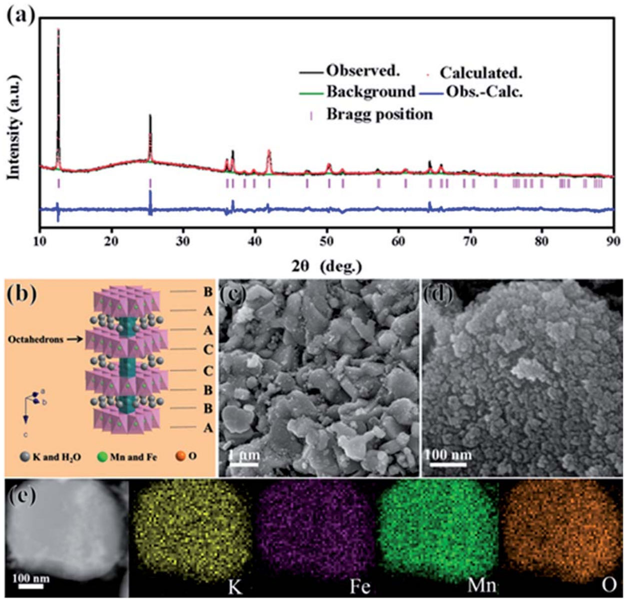

Fig. 2 (a) Refined XRD patterns of KFM ($R_{WP} = 6.73\%$, $R_p = 3.62\%$, and $\chi^2 = 3.629$). (b) The crystal structure of KFM. (c and d) SEM images of KFM with different magnifications. (e) Elemental mapping images of KFM.

centrifuging step were recorded. The ash was divided into two parts and was naturally cooled to room temperature in an argon-filled glovebox and open air, respectively. And then the ash was immediately characterized with XRD measurements; it could be found that the characteristic peaks of both the ash samples are similar to the KFM ones except for the low crystallinity and right shift phenomenon of the peaks as shown in Fig. S2.† The peak deviation originated from the *c* lattice extension/contraction and is mostly related to the absorption/de-absorption of water molecules.[22] The peak deviation of the ash sample cooled down in an argon-filled glovebox is more obvious than that of the open air one and it could be inferred that both the air cooling and water rinsing processes involve the absorption of water in the structure of KFM, and the air cooling might contribute a relatively high quantity. Even though the peaks of the ash are similar to that of KFM, the water rinsing is still necessary as a colorful transparent solution of the by-product could be obtained during the centrifugation process as shown in Fig. S3.† It should be noted that the 500 °C heated KFM sample shown in Fig. S1,† was also protected and cooled down in an argon-filled glovebox, but the peak shift phenomenon is not as obvious as in the ash. This phenomenon might mostly originate from the increased water sensitivity after the removal of the by-product by centrifugation.

To examine the stability of KFM in air, fresh KFM samples are stored both in ambient air and an argon-filled glovebox for one week. Through comparison of XRD patterns, it's hard to find any trace of other phases (Fig. S4†), and thus it's deduced that there is no side reaction between the KFM materials and the H_2O/CO_2 in air. What's more, it should be noticed that the electrodes for electrochemical tests were prepared with the water-based binder (carboxymethyl cellulose) which is quite different from most cases of cathode materials for NIBs with an organic liquid-based binder (mainly polyvinylidene fluoride).[6,9–14,17–21] From the observation that no drastic change is found between the raw material and the electrode, it's deduced that no influence could originate from the presence of plenty of H_2O, and the impact of H_2O in ambient air seems also negligible from this point of view.

The morphology and particle size of KFM are observed by scanning electron microscopy (SEM) (Fig. 2c and d). It can be seen that the distribution of the particle size is in the range of 0.5–1 μm and the surface is fairly rough and is covered by smaller agglomerates with diameter sizes around 10 nm. Furthermore, the thickness of the agglomerate surface layer is about 30–50 nm as confirmed using a transmission electron microscope (TEM) as shown in Fig. S5.† Elemental mapping images show the homogeneous distributions of potassium, iron, manganese and oxygen (Fig. 2e), further confirming the successful synthesis of KFM.

Furthermore, X-ray photoelectron spectroscopy (XPS) analysis was employed to further examine the chemical valence states of the transition metal elements (Fig. 3). The KFM shows peaks at 711.27 and 725.27 eV for Fe 2p3/2 and Fe 2p1/2, respectively. The results indicate that the valence state of Fe is +3; meanwhile the satellite peak that appeared at 719.22 eV is also a typical characteristic of Fe^{3+}.[26] In addition, the binding energies of Mn 2p3/2 and Mn 2p1/2 centered at 642.65 and 654.22 eV show that the valence state of Mn is +4 and are in good agreement with the reported data on MnO_2.[27]

2025 coin-type cells with Na foil as the counter electrode were first assembled to explore the Na ion storage abilities of KFM. Fig. 4a shows the cyclic voltammetry (CV) curves of KFM at a scan rate of 0.1 mV s^{-1} in the voltage range of 1.6–3.8 V. Different from the initial scan which has some minor peaks caused by the side reactions, the subsequent scans (2nd to 10th) exhibit regularity and the two cathodic peaks between 2 and 2.5 V pair with the intense anodic peak at about 2.6 V. The unmatched peak number should be explained by the polarization. From the simple and regular CV curves, it's deduced that drastic structural evolution has not happened during the Na ion insertion/desertion process. The redox peaks involve the valence changes of both Fe and Mn and are affirmed by the *ex situ* XPS method as shown in Fig. S6.† Galvanostatic discharge–charge curves of KFM at 10 mA g^{-1} between 1.6 and 3.8 V are displayed in Fig. 4b. An initial discharge capacity of 125.7 mA h g^{-1} is delivered which corresponds to 0.5 Na ion insertion per formula unit (as there are no Na ions in the layers

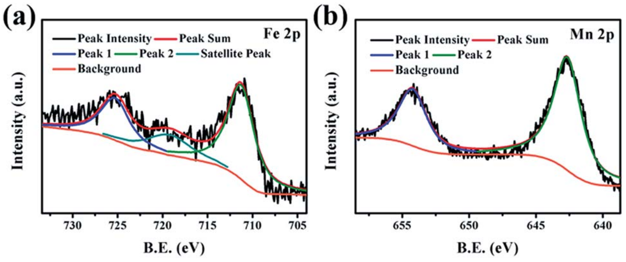

Fig. 3 (a) Fe 2p and (b) Mn 2p XPS spectra of KFM.

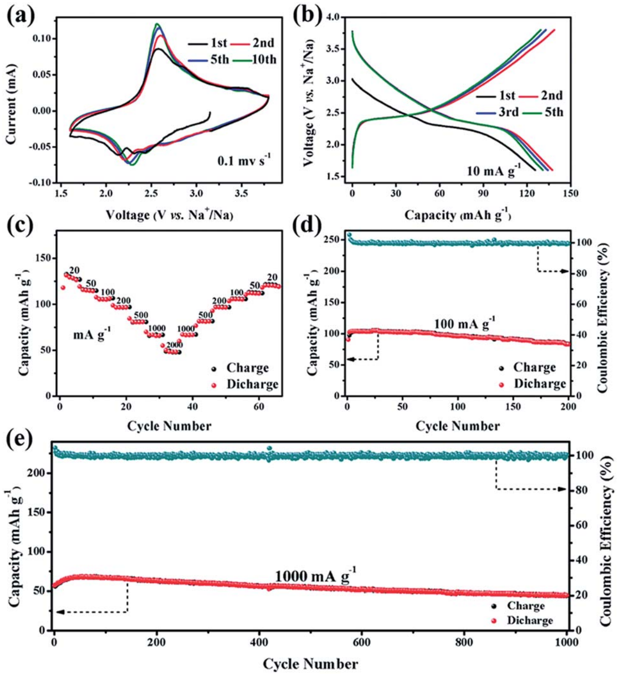

Fig. 4 (a) CV curves of KFM at 0.1 mV s^{-1} (*vs.* Na^+/Na). (b) Discharge/charge curves of KFM at 10 mA g^{-1}. (c) Rate performance of KFM. (d and e) The cycle performances of KFM at 100 and 1000 mA g^{-1}, respectively.

of KFM, it's defined here that the first cycle is the electrochemical activation of KFM with only the discharge process for calculating CE in the later cycles with the formula CE = discharge capacity/charge capacity). During the second cycle, capacities of 138.7 and 137.5 mA h g^{-1} are obtained for the charge and discharge processes, and meanwhile the higher desertion–insertion capacities than the initial cycle indicate that the K ions are also involved in the subsequent cycles. The maintenance of the shape of the curves is an evident proof that an analogical ion insertion/desertion process occurs in subsequent cycles. Fig. 4c shows the rate cycling behavior of the KFM electrode. The cell delivers discharge capacities of approximately 129, 115, 105, 97, 81, 67 and 48 mA h g^{-1} at sequential rates of 20, 50, 100, 200, 500, 1000 and 2000 mA g^{-1}, respectively. When the rate is reset step-wise from 2000 to 20 mA g^{-1}, the capacity value at each rate remained stable and high capacities over 120 mA h g^{-1} are still delivered at 20 mA g^{-1}.

The cycling performance of KFM was first investigated at 100 mA g^{-1} as shown in Fig. 4d (the corresponding discharge–charge curves are displayed in Fig. S7†). The KFM demonstrates a discharge capacity of 90.5 mA h g^{-1} for the 1st cycle and a gradually activated process appears, where a maximum value of 105.4 mA h g^{-1} is obtained for the 28th cycle. After 200 cycles, the capacity retention is 92% corresponding to reversible charge/discharge capacities of 83.7/83.2 mA h g^{-1}. It's worth noting that the CEs are approximately 100% during the whole cycles. Moreover, the KFM electrode also exhibits a satisfactory electrochemical performance at a higher rate of 1000 mA g^{-1} where a highest discharge capacity of 68.1 mA h g^{-1} (50th cycle) together with a retained discharge capacity of 44.5 mA h g^{-1} (78.5% capacity retention) after 1000 cycles is delivered (Fig. 4e and S8†). The CEs of the electrode still remain at *ca.* 100% during cycling, indicative of a highly reversible insertion/desertion mechanism. It should be stressed that the as-synthesized KFM is a hydrated phase but no obvious disadvantage is found during the cycles. In recent years, some hydrated phases such as $FeF_3 \cdot 0.5H_2O$, $Na_2Fe(SO_4)_2 \cdot 2H_2O$, and $Na_{0.71}MnO_2 \cdot 0.25H_2O$ have also emerged and been selected as cathode materials for Na ion batteries.[28–30] It's inferred that there could be some minor contamination of the electrolyte by the crystal water but it would not play a key role in cycling degradation. The water might also contribute a little part of the specific capacity when considering cathode electrolyte interface film formation on KFM.

The electrochemical performance of the materials obtained after post heat treatment at 200 °C was also tested for comparison (Fig. S9a and b†). No great difference could be found between the conventional KFM and the 200 °C heated one. This phenomenon should be explained by the fact that even though the water could be removed during the heating process, the water could be resorbed by the structure during the cooling process. Also, the electrode making process involved water as a binder solvent which would make the heated sample finally have no great difference compared to the conventional KFM. Actually, NIBs are very sensitive to water content which could easily deteriorate the electrolyte and sodium anodes. In our future work, it's a very meaningful thing to synthesize the pure K–Fe–Mn–O compound without crystal water and without any contact with water that might demonstrate better Na ion storage abilities.

An *ex situ* XRD method was employed to further understand the structure transformation mechanism during the Na ion insertion/desertion reactions through recording electrodes with different depths of discharge and charge at 10 mA g^{-1} (Fig. 5a). The electrodes of different depths were taken from the cells in an argon atmosphere and sealed in sample holders equipped with Kapton film windows. The bottom black line in Fig. 5b represents the peaks from the background, namely, the Kapton film, the aluminum collector and the sample holder. During the first discharge from the open circuit potential (A) to 2.35 V (B), the peak at 12.62° (0 0 −3) corresponding to the interplanar distance of 7.0097 Å shifts to a higher angle of 12.80° and an

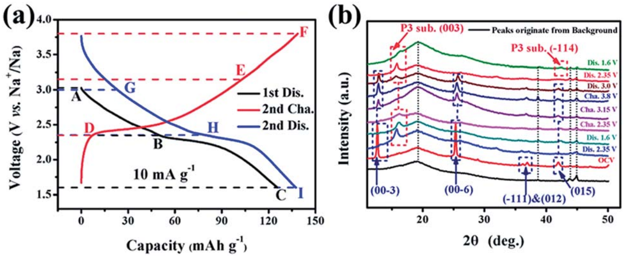

Fig. 5 (a) The discharge/charge curves of KFM (10 mA g^{-1}) with the selected depths of discharge/charge (A to I). (b) The corresponding XRD patterns of different stages in (a) (bottom to top—A to I).

obvious new peak at 15.83° corresponding to an interplanar distance of 5.59 Å is found. The peak shift phenomenon should be caused by some loss of crystal water, and the new peak should be still indexed to the P3 type structure. Even the angle and the interplanar distance are also close to those of the P2-type Na_xMeO_2; however the transformation from P3 to P2 needs the breaking and reforming of Me–O bonds and can't be achieved under such common reaction conditions.[17,31–34] At the end of the first discharge (C, 1.6 V), the pristine (0 0 −3) lattice plane is not detectable, and the new P3 substitution peak shifts to a higher angle of 16.24° (an interplanar distance of 5.45 Å). The usual phase transformation (P3 to O3 in the lower voltage range) in the O3-type Na_xMeO_2 cases does not occur as the characteristic peak of O3-type Na_xMeO_2 around at 40° has not been detected,[12,18,19] and thus the new shifted position is still a representative of P3. When charged to 2.35 V (D) and 3.15 V (E) in the second cycle, the pristine structure is gradually formed and the P3 substitution disappears. At the cut-off voltage of charge of 3.8 V (F), the XRD curves show nearly the same shape as the electrode before cycling which is one powerful piece of evidence that the reversible chemical reaction occurs. Next, when the electrode is discharged to 3.0 V (G), 2.35 V (H) and 1.6 V (I), it shows the same trend as the first discharge and the reverse process of the second charge process. The XRD curves of the electrodes at the end of charge/discharge of the 5th (performed at 10 mA g^{-1}), 120th (performed at 100 mA g^{-1}) and 1000th (performed at 1000 mA g^{-1}) cycles are also given as shown in Fig. S10.† It's found that as the electrode is charged to 3.8 V, traces of P3 substitution are still detectable and this phenomenon is particularly obvious at the end of charge in the 120th cycle. It should be explained by the gradual substitution of K ions by Na ions with a smaller radius in KFM and is also supported by the almost invisible K XPS after 120 cycles as shown in Fig. S11.† However, at the end of discharge the original P3-type structure is undetectable both for the 5th and 120th cycle and the main peak of P3 substitution also shifts higher to about 16.24° which is corroborative evidence that the interplanar layers of P3 substitution shrink and the primitive P3 converts to P3 substitution during the insertion of Na ions. From the electrodes at the 1000th cycle state, it could be observed that the original P3 phase has totally disappeared, and the charge–discharge process is also accompanied by peak shifts of the P3 substitution (Fig. S10c†), this difference between the peaks of the 1000th cycle and those of Fig. S10a and b† might originate from the complete disappearance of K ions and water molecules in the original P3 layer structure. Also, some unknown weak signals between 29 and 37° are ultimately detected, and these might originate from some inevitable side reactions between the electrolyte and the electrode material. The SEM images of the KFM at the end of charge/discharge for 120 cycles are also given (Fig. 6). It's observed that except for some tiny volume expansion at the end of discharge, no difference of particle size and shape is found compared with the raw sample (Fig. 2c and d). This is also evidence that the insertion/desertion mechanism occurs but the conversion/deconversion mechanism accompanied by enormous volume expansion and even crushing of the active materials does not occur. To exclude the coverage influences caused by the Kapton films, the electrodes without Kapton films and sample holders were also tested for comparison (Fig. S12†). In the air exposed *ex situ* XRD data, it can be obviously observed that the above-mentioned broad signals did not appear. So it's deduced that the broad background signals in Fig. 5b simply originate from the Kapton films but not from water or structural disorder. Compared to the result of Fig. 5b, the signals of the original P3 phase have reduced in intensity and those of the P3 substitution have increased in intensity (Fig. S12†), this phenomenon might be caused by the instabilities of the charged/discharged original P3 phase in ambient air. According to the above results, a simple structure transformation from P3 (interplanar distance of 7.0097 Å) to P3 substitution (interplanar distance of 5.45 Å) occurs when KFM is employed as the cathode of NIBs, and it should also be a reasonable explanation for the remarkable electrochemical performance as mentioned above. Although the conversion from primitive P3 to P3 substitution is found to be irreversible at the end of cycle life, the new P3 substitution remains stable and the transformation mechanism here is much simpler than those of the OP4–P2–P′2 and O1–P3–O3 transformations in P2 and O3-type Na_xMeO_2, respectively.[16]

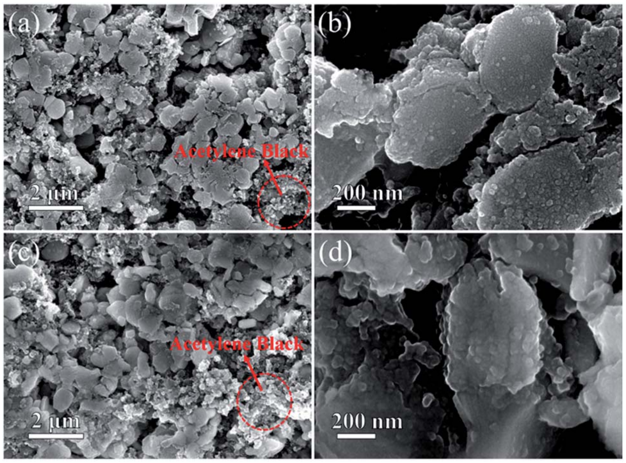

Fig. 6 (a and b) SEM images of the KFM at the end of charge in the 120th cycle. (c and d) SEM images of the KFM at the end of discharge in the 120th cycle.

Inspired by the superior Na-ion storage performances presented above in half cells, prototype Na-ion full batteries were assembled using the layered KFM as the cathode and un-optimized sodiated-Sb_2O_3 as the anode. Typical discharge–charge curves of the full cell between 1 and 3.2 V at different rates are shown in Fig. 7a, and discharge capacities of 117.3, 100.4, 93.4, 84.4, 70.3, 57.5 and 42.8 mA h g^{-1} are exhibited at current densities of 20, 50, 100, 200, 500, 1000 and 2000 mA g^{-1}, respectively. The average voltages are in the range of 1.88 to 2.17 V. Interestingly, the maximum energy density and power density are calculated to be 220.5 W h kg^{-1} and 4340 W kg^{-1}, respectively, based on the cathode mass. The full cell demonstrates high CEs close to 100% at all rates, especially it still demonstrates a high CE of 98.8% even at a very high current rate (2000 mA g^{-1}) which is uncommon for NIBs and much

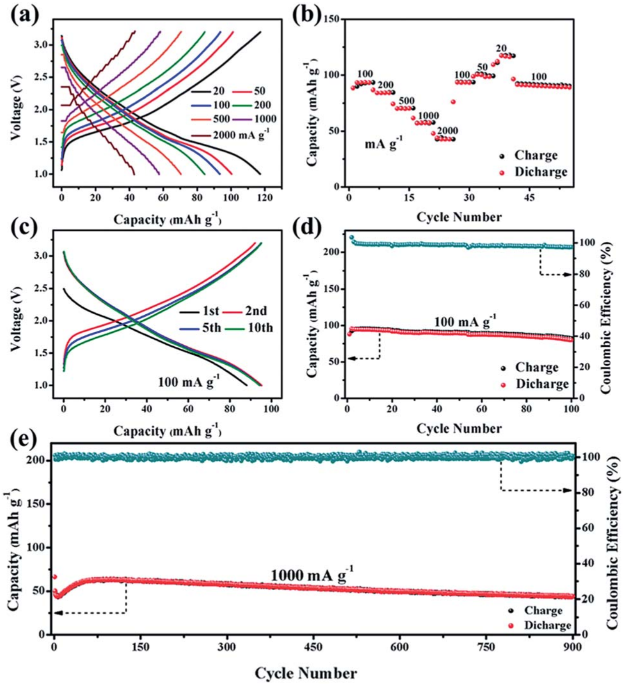

Fig. 7 (a) Charge–discharge curves of the KFM/Na_x-Sb_2O_3 full battery at various current densities. (b) The rate performance of the full battery. (c andd) Discharge–charge curves and cycle performance of the full battery at 100 mA g^{-1}. (e) Long cycle performance of the full battery at 1000 mA g^{-1}.

higher than those of the commercialized Na–S batteries (75–85%).[35] Furthermore, from the rate performance shown in Fig. 7b, it's found that the drastic capacity loss phenomenon does not happen despite higher current densities of 1000 and 2000 mA g^{-1}. The discharge–charge curves and the cycle performance at a fixed value of 100 mA g^{-1} are displayed in Fig. 7c and d, and the shape of the curves remains steady and a discharge capacity of 80.0 mA g^{-1} (90.8% retention) is still exhibited after 100 cycles. Encouraged by the long lifespan of the half cell and the excellent rate performance of the full cell, further testing at an unusual high current rate for the full cell (1000 mA g^{-1}) is performed as shown in Fig. 7e and S13.† The cell exhibits a high initial discharge capacity of 66.1 mA h g^{-1} and still has a capacity of 43.9 mA h g^{-1} after 900 cycles which are uncommon properties that have never been reported for Na-ion full batteries. In this full cell system, the KFM electrode also has great recycling value, *i.e.*, it could be still further utilized after hundred cycles.

The cycle performance of the full battery shown in Fig. 7d is also tested as shown in Fig. 8a and b. The discharge capacity gradually decreases from 79.8 to 54.9 mA h g^{-1} and the coulombic efficiency gradually decreases from 97.3% to 95.5% (101st to 199th). However, when the battery is detached and the cycled KFM electrode is further assembled with the fresh Na_x–Sb_2O_3 electrode, the electrode is able to give stable cycle performance, high coulombic efficiencies of nearly 100% and high discharge capacities of 61.2, 81.1 and 104.8 mA h g^{-1} at 100, 50 and 20 mA g^{-1}, respectively (Fig. 8c and d). The result

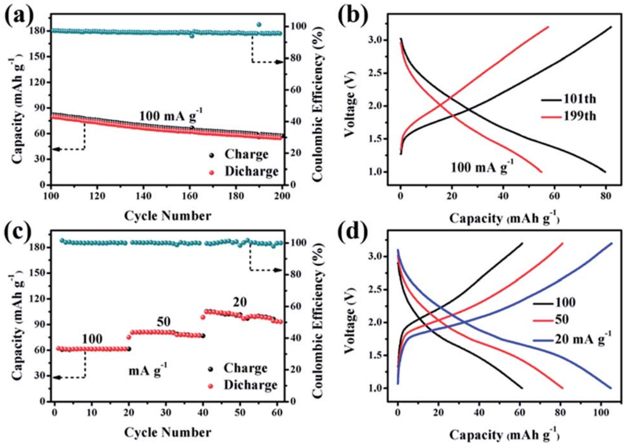

Fig. 8 (a and b) Cycle performance (101st to 199th) and discharge–charge curves (101st and 199th) of the KFM/Na_x–Sb_2O_3 full battery at 100 mA g^{-1}. (c and d) Cycle performance and discharge–charge curves of the cycled-KFM/Na_x–Sb_2O_3 full battery at various current densities.

indicates that the full battery system of KFM/Na_x–Sb_2O_3 provides the KFM electrode recycling ability, and this is very meaningful for the practical application of KFM/Na_x–Sb_2O_3 batteries in the future. Besides the realization of full cells, our result also shows a distinct lifespan advantage at high current density (characteristic of high power density) compared with the other cathodes as listed in Table S3.† Table S4† lists the comparison between KFM and some representative state-of-the-art NIB cathode materials together with our previous study on another P3-type $K_{0.33}Co_{0.53}Mn_{0.47}O_2\cdot 0.39H_2O$;[36] it could be found that KFM is still competitive especially in the case of full cells with impressive long cycle performance and considerable average potential.

Conclusions

In summary, as a proof-of-concept experiment, a novel potassium layered transition-metal oxide, KFM (a representative example of the big P3-type K_xMeO_2 family), with a rare P3-type structure is synthesized and employed as a low-cost, air-stable and Co/Ni-free cathode in NIBs for the first time. Unexpectedly, the KFM exhibits superior electrochemical performances, including a high specific capacity of 137.5 mA h g^{-1} and excellent cycling performance (up to 1000 cycles) with *ca.* 100% CE. Furthermore, a very highly efficient prototype NIB was first realized using a KFM cathode and an un-optimized sodiated-Sb_2O_3 anode, which shows a maximum energy density and power density of 220.5 W h kg^{-1} and 4340 W kg^{-1}, respectively, a high round-trip energy efficiency of *ca.* 100%, and excellent cycling stability (over 900 cycles even at a high current density of 1000 mA g^{-1}). Moreover, a new structure transformation mechanism is also found here by an *ex situ* XRD method which indicates that the P3-type structure of KFM converts to a P3 substitution and undesirable multiple irreversible phase transitions observed in P2 and O3-type Na_xMeO_2 have not happened. Accelerating the process of NIB industrialization needs particular attentions on low cost and excellent Na ion storage abilities of cathode materials, and thus we believe that the very promising performance of KFM (made from environmentally friendly and low-cost elements) even in prototype batteries will open new avenues and inspire more research interest for practical application of P3-type K_xMeO_2 in NIBs for large-scale electrical energy storage.

Conflicts of interest

There are no conflicts to declare.

Acknowledgements

This work is financially supported by the National Natural Science Foundation of China (51522101, 51471075, 51631004 and 51401084), Specialized Research Fund for the Doctoral Program of Higher Education of China (20110061120040) and Program for Innovative Research Team (in Science and Technology) in University of Jilin Province.

Notes and references

1 Q. Zhang, E. Uchaker, S. L. Candelaria and G. Cao, *Chem. Soc. Rev.*, 2013, **42**, 3127.
2 F. Cheng, J. Liang, Z. Tao and J. Chen, *Adv. Mater.*, 2011, **23**, 1695.
3 L. Zhao, J. Zhao, Y.-S. Hu, H. Li, Z. Zhou, M. Armand and L. Chen, *Adv. Energy Mater.*, 2012, **2**, 962.
4 D. Su, S. Dou and G. Wang, *Chem. Mater.*, 2015, **27**, 6022.
5 W. Zhang, Y. Liu, C. Chen, Z. Li, Y. Huang and X. Hu, *Small*, 2015, **11**, 3822.
6 K. Kaliyappan, J. Liu, A. Lushington, R. Li and X. Sun, *ChemSusChem*, 2015, **8**, 2537.
7 Y. Liu, N. Zhang, L. Jiao, Z. Tao and J. Chen, *Adv. Funct. Mater.*, 2015, **25**, 214.
8 H. Wang, P. Hu, J. Yang, G. Gong, L. Guo and X. Chen, *Adv. Mater.*, 2015, **27**, 2348.
9 Y. Fang, L. Xiao, J. Qian, X. Ai, H. Yang and Y. Cao, *Nano Lett.*, 2014, **14**, 3539.
10 Y. Fang, L. Xiao, X. Ai, Y. Cao and H. Yang, *Adv. Mater.*, 2015, **27**, 5895.
11 J. Qian, M. Zhou, Y. Cao, X. Ai and H. Yang, *Adv. Energy Mater.*, 2012, **2**, 410.
12 D. Yuan, X. Liang, L. Wu, Y. Cao, X. Ai, J. Feng and H. Yang, *Adv. Mater.*, 2014, **26**, 6301.
13 Y. Wang, R. Xiao, Y.-S. Hu, M. Avdeev and L. Chen, *Nat. Commun.*, 2015, **6**, 6954.
14 Y. Li, Z. Yang, S. Xu, L. Mu, L. Gu, Y.-S. Hu, H. Li and L. Chen, *Adv. Sci.*, 2015, **2**, 1500031.
15 H. Pan, Y.-S. Hu and L. Chen, *Energy Environ. Sci.*, 2013, **6**, 2338.
16 X. Xiang, K. Zhang and J. Chen, *Adv. Mater.*, 2015, **27**, 5343.
17 P.-F. Wang, Y. You, Y.-X. Yin, Y.-S. Wang, L.-J. Wan, L. Gu and Y.-G. Guo, *Angew. Chem., Int. Ed.*, 2016, **55**, 7445.
18 P.-F. Wang, Y. You, Y.-X. Yin and Y.-G. Guo, *J. Mater. Chem. A*, 2016, **4**, 17660.
19 H. Guo, Y. Wang, W. Han, Z. Yu, X. Qi, K. Sun, Y.-S. Hu, Y. Liu, D. Chen and L. Chen, *Electrochim. Acta*, 2015, **158**, 258.
20 S. Kalluri, K. H. Seng, W. K. Pang, Z. Guo, Z. Chen, H.-K. Liu and S. X. Dou, *ACS Appl. Mater. Interfaces*, 2014, **6**, 8953.
21 L. Mu, S. Xu-, Y. Li, Y.-S. Hu, H. Li, L. Chen and X. Huang, *Adv. Mater.*, 2015, **27**, 6928.
22 R. Chen, P. Zavalij and M. S. Whittingham, *Chem. Mater.*, 1996, **8**, 1275.
23 Y. Liu, Y. Qiao, W. Zhang, H. Xu, Z. Li, Y. Shen, L. Yuan, X. Hu, X. Dai and Y. Huang, *Nano Energy*, 2014, **5**, 97.
24 C. Delmas, C. Fouassier and P. Hagenmuller, *Physica B+C*, 1980, **99**, 81.
25 D. Buchholz, L. G. Chagas, C. Vaalma, L. Wu and S. Passerini, *J. Mater. Chem. A*, 2014, **2**, 13415.
26 Q. An, F. Lv, Q. Liu, C. Han, K. Zhao, J. Sheng, Q. Wei, M. Yan and L. Mai, *Nano Lett.*, 2014, **14**, 6250.
27 L. Li, A.-R. O. Raji and J. M. Tour, *Adv. Mater.*, 2013, **25**, 6298.
28 C. Li, C. Yin, L. Gu, R. E. Dinnebier, X. Mu, P. A. van Aken and J. Maier, *J. Am. Chem. Soc.*, 2013, **135**, 11425.
29 P. Barpanda, G. Oyama, C. D. Ling and A. Yamada, *Chem. Mater.*, 2014, **26**, 1297.
30 K. W. Nam, S. Kim, E. Yang, Y. Jung, E. Levi, D. Aurbach and J. W. Choi, *Chem. Mater.*, 2015, **27**, 3721.
31 X. Chen, X. Zhou, M. Hu, J. Liang, D. Wu, J. Wei and Z. Zhou, *J. Mater. Chem. A*, 2015, **3**, 20708.
32 M. D. Slater, D. Kim, E. Lee and C. S. Johnson, *Adv. Funct. Mater.*, 2013, **23**, 947.
33 K. Kubota, N. Yabuuchi, H. Yoshida, M. Dahbi and S. Komaba, *MRS Bull.*, 2014, **39**, 416.
34 N. Yabuuchi, K. Kubota, M. Dahbi and S. Komaba, *Chem. Rev.*, 2014, **114**, 11636.
35 B. Dunn, H. Kamath and J.-M. Tarascon, *Science*, 2011, **334**, 928.
36 S. Wang, T. Sun, S. Yuan, Y.-H. Zhu, X.-B. Zhang, J.-M. Yan and Q. Jiang, *Mater. Horiz.*, 2017, **4**, 1122.